Systematic approach to damping ring design

Paul Emma and Tor Raubenhemier
Stanford Linear Accelerator Center, Stanford University, Stanford, California 94309

(Received 6 September 2000; published 7 February 2001)

A design process is described for damping rings in a linear collider where the competing requirements of small equilibrium emittance and fast damping of the injected phase space are needed. A systematic approach to the determination of the basic ring parameters is described. In addition, qualitative consideration is given to minimizing the system cost. The approximate interdependencies of the various lattice parameters are derived and arguments for the parameter choices are presented. In addition, many useful expressions are derived for a theoretical minimum emittance lattice. The design of the damping rings for the Next Linear Collider design are used as examples throughout.

DOI: 10.1103/PhysRevSTAB.4.021001 PACS numbers: 29.20.Dh, 29.17.+w, 41.75.Ht

I. INTRODUCTION

Future electron/positron linear colliders [1] require beams with very small transverse emittances to attain their luminosity goals. Unfortunately, these desired emittances are many orders of magnitude smaller than those produced by “conventional” particle sources such as subharmonic bunchers for polarized electron beams or electromagnetic cascades for positron sources. rf guns have the potential to produce beams that are closer to that required. However, at the present time, rf guns are not able to produce the desired beams; the combination of very small emittance and high beam polarization has not yet been achieved in electron rf guns and a positron rf gun has not been developed.

A number of techniques have been developed to decrease the phase space volume of a particle beam, including stochastic cooling, electron cooling, ionization cooling, laser damping, and damping due to synchrotron radiation. With present technology, only the last technique can attain the very fast damping rates that are desired without significant dilution of the phase space; the other processes are orders of magnitude too slow or cause an unacceptable dilution of the longitudinal phase space. Thus, the bunch trains in a linear collider are generated with conventional sources and then injected into a damping ring where synchrotron radiation damping is used to damp the large emittance of the injected beams. The required emittances are not much smaller than those produced in the current generation of synchrotron light sources. However, to produce the desired beams at the collider repetition rate while constraining the cost of the damping rings, the rings must also have very fast damping rates. Unfortunately, this requirement is frequently in conflict with the requirement of small equilibrium emittances which limits the design parameter space.

In this paper, we present a systematic approach to the design of a damping ring. This design procedure is an extension of those described in Refs. [2–4]. Starting from a few global parameters, such as the injected and extracted emittance and the repetition rate, most of the damping ring parameters can be determined. However, we also consider constraints due to cost, dynamic aperture, momentum compaction, alignment tolerances, kicker limitations, and spin preservation, all of which further constrain the design. This systematic approach can be easily automated which then allows for quantitative cost and systems optimization beyond the qualitative guidelines presented here.

In the following, the design procedure will be described in the order in which it is easiest to implement for an automated calculation starting from the primary input parameters. The basic layout of the ring that we consider is a racetrack with two 180° arcs separated by straight sections that are used for injection/extraction, the rf cavities, and damping wigglers. The ring circumference is based on the bunch train length and kicker limitations while the store time is a compromise between looser vertical alignment tolerances and unnecessary damping. The beam energy is chosen based on many aspects including spin preservation, reasonable dipole fields, momentum compaction, damping time, and damping wiggler length. A damping wiggler is introduced in order to increase the damping rate without going to a higher, more difficult energy. The arcs are composed of theoretical minimum emittance (TME) cells [5] which are well suited to a damping ring of this sort, and the optical design of the TME cells is optimized in order to produce maximum dispersion to improve the dynamic aperture and momentum compaction. Finally, the design process will be illustrated with examples from the Next Linear Collider (NLC) main damping ring (MDR) with references to the NLC positron predamping ring (PDR) when useful to illustrate significant differences; the PDR is used to damp the very large emittance positron beam before it is injected into the positron MDR.

II. INPUT PARAMETERS

The primary input parameters are those that define the length of the bunch train and those that define the emittance and damping requirements of the ring. Parameters

1098-4402/01/4(2)/021001(16)$15.00

TABLE I. Parameters which determine the minimum circumference and damping requirements of the ring. The values listed here are for the NLC e^+/e^- MDR and the e^+ PDR.

Parameter	Symbol	PDR	MDR
Number of bunches per train	N_b	95	95
Bunch to bunch spacing within train [ns]	τ_b	2.8 or 1.4	2.8 or 1.4
Minimum gap between trains for kicker rise/fall [ns]	τ_k	100	65
Maximum collider repetition rate (of trains) [Hz]	f	120	120
Injected x and y emittance (norm., rms) [μm]	$\gamma\varepsilon_{x,y0}$	<42 000	<150
Extraction horizontal emittance desired (norm., rms) [μm]	$\gamma\varepsilon_x$	<150	<3
Extraction vertical emittance desired (norm., rms) [μm]	$\gamma\varepsilon_y$	<150	<0.03

for the NLC damping rings are listed in Table I where the first three parameters determine the minimum ring circumference, while the last four determine the damping requirements. Some of these values are set by parameters of the collider such as emittance of the injector, collider luminosity, and collision repetition rate, while others are set by technical limitations, such as a reasonable rise and fall time of the ring injection and extraction kickers, which can limit either the spacing between bunches or the gaps between bunch trains depending on the mode of injection and extraction.

In addition to these primary parameters, the ring must also be designed with consideration of an adequate dynamic aperture, reasonable peak currents to limit single bunch instabilities as well as intrabeam scattering and space charge effects, and a reasonably large momentum compaction, and it must be optimized with regards to cost. The reason for the first item is obvious—undamped beams are continually being injected into the damping ring and the dynamic aperture must be large enough to prevent particle loss which will cause both large radiation loads, because of the high average power of the injected beams, and difficulties in the downstream linacs due to variations in the bunch charge and beam loading. Usually, we request a transverse aperture, including errors, that is greater than 10 times the injected beam size and an energy aperture of a few percent. However, the optimization of the dynamic aperture is beyond the scope of this report and here we simply apply a few rules in the design process that should make it easier to attain a large aperture.

Next, the limitations on the peak current arise from the single bunch longitudinal instability thresholds, the incoherent space charge tune shift, and the intrabeam scattering. All three of these effects are straightforward to estimate from analytic formulas. They are all eased with longer bunches, which is one reason to design the ring with a large momentum compaction factor. Another limitation on the momentum compaction factor is related to the stability requirements. The damping ring must produce very stable beams in both the transverse and longitudinal phase spaces. In a storage ring with synchrotron radiation, the beam energy will change with changes to the ring circumference, which can arise from thermal changes or ground motion effects, as

$$\frac{\Delta E}{E} = \frac{1}{\alpha}\frac{\Delta C}{C}\,. \tag{1}$$

In a strong focusing, low emittance, lattice this can impose a very tight constraint on ring circumference errors. In the NLC rings, we have determined a limit of $\alpha > 5 \times 10^{-4}$; this makes it straightforward to attain a 5 mm bunch length and sets a tolerance on the circumference stability of $|\Delta C| \approx 15\ \mu$m, which can be partially stabilized with a compensating chicane [6], as will be discussed.

Finally, the rings must be optimized with regard to cost. In this paper, the cost aspect is addressed by attempting to reduce the size and number of components such as the wiggler length, the number of TME cells, and the number of quadrupole magnets per cell. However, it is also possible to include detailed cost information in the design procedure and then use the procedure to optimize the ring and overall system costs.

III. VERTICAL EMITTANCE AND STORE TIME

For a flat beam, achieving the very small extracted vertical emittance is the most challenging aspect of ring design and construction. Many of the most demanding tolerances, such as sextupole and quadrupole magnet alignment, are set by the chosen equilibrium vertical emittance $\varepsilon_{y\mathrm{e}}$. The extracted vertical emittance is a combination of the damped injection emittance and the error-driven equilibrium emittance,

$$\varepsilon_y = \varepsilon_{y0}e^{-2N_\tau} + (1 - e^{-2N_\tau})\varepsilon_{y\mathrm{e}}\,, \tag{2}$$

where N_τ is the store time per train in units of damping time constants ($N_\tau \equiv \Delta t/\tau_y$) and the other symbols are described above or in Table I. For given values of injection and extraction emittance, the choice of equilibrium emittance is a balance between looser vertical alignment tolerances (i.e., larger $\varepsilon_{y\mathrm{e}}$) and a longer relative store time (i.e., larger N_τ),

$$\frac{\varepsilon_{y\mathrm{e}}}{\varepsilon_y} = \frac{e^{2N_\tau} - \varepsilon_{y0}/\varepsilon_y}{e^{2N_\tau} - 1}\,. \tag{3}$$

Loosening the vertical alignment tolerances amounts to increasing the equilibrium emittance $\varepsilon_{y\mathrm{e}}$ toward the extracted emittance ε_y. Figure 1 shows the ratio of equilibrium emittance to extracted emittance $\varepsilon_{y\mathrm{e}}/\varepsilon_y$ (plotted for the NLC value of $\gamma\varepsilon_y = 0.03\ \mu$m) versus relative store time N_τ.

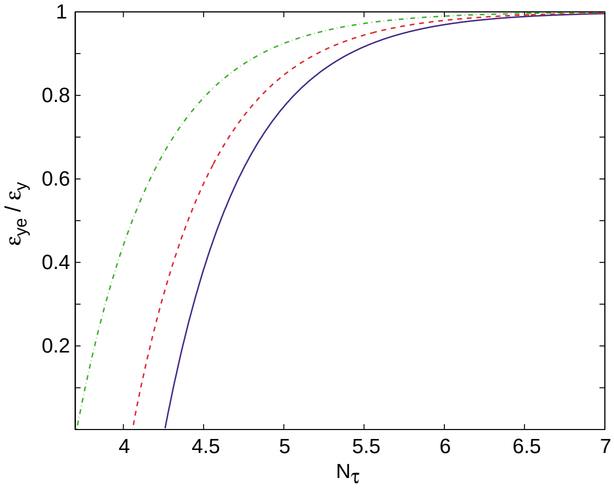

FIG. 1. (Color) Equilibrium vertical emittance divided by an extracted emittance of $\gamma\varepsilon_y = 0.03$ μm versus relative store time N_τ for initial emittance values of $\gamma\varepsilon_{y0} = 150$ μm (solid line), 100 μm (dashed line), and 50 μm (dot-dashed line). A reasonable choice that adequately loosens tolerances is in the region $0.6 < \varepsilon_{ye}/\varepsilon_y < 0.9$.

The point at which $\varepsilon_{ye}/\varepsilon_y$ crosses zero is not important; it is simply the number of damping times where it is impossible to achieve a value of $\gamma\varepsilon_y = 0.03$ μm, from the given initial emittance.

As seen in Fig. 1, increasing N_τ eventually has no significant effect on $\varepsilon_{ye}/\varepsilon_y$, although it complicates the ring design, forcing faster and faster damping. Since the vertical alignment tolerances scale with $\varepsilon_{ye}^{1/2}$, it seems reasonable to choose $0.6 < \varepsilon_{ye}/\varepsilon_y < 0.9$. Larger values of N_τ force a faster damping rate with little benefit in terms of the alignment tolerances, while smaller values tighten the tolerances unnecessarily.

There are two other considerations when choosing these parameters: the stability of the extracted emittance and the minimum vertical emittance set by the opening angle of the synchrotron radiation. In general, the beam emittance and trajectory coming from the low energy injector will fluctuate—the low energy beam is very sensitive to small changes in trajectory, bunch length, and charge. Thus, one purpose of the damping ring is to damp these transients and produce a more stable beam for the downstream systems. For this reason, one would like to have $\varepsilon_{ye}/\varepsilon_y$ relatively large. On the other hand, it does not make sense to choose N_τ so that the injected beam is damped well below the minimum vertical emittance set by the opening angle of the synchrotron radiation. This can be estimated as [7]

$$\Delta\gamma\varepsilon_y \approx 0.24 J_\varepsilon \langle\beta_y\rangle \frac{\sigma_\delta^2}{\gamma}, \qquad (4)$$

where J_ε (≈ 2) is the longitudinal damping partition number, $\langle\beta_y\rangle$ (≈ 5 m) is the mean vertical beta function, and σ_δ ($\approx 0.1\%$) is the rms relative energy spread at extraction. For typical values (in parentheses) at 2 GeV, this emittance limit is $\Delta\gamma\varepsilon_y \approx 0.0005$ μm, or 2% of the desired NLC MDR extraction emittance. At $N_\tau \approx 6.3$ an initial emittance of $\gamma\varepsilon_{y0} \approx 150$ μm will damp to this value implying that such a long store time is probably not useful.

The choice for the NLC main damping ring is made, somewhat arbitrarily, at $\varepsilon_{ye}/\varepsilon_y \approx 0.67$. This choice damps away most of the injection transients and attains tolerances which are just 18% tighter than for $N_\tau \to \infty$. This sets $N_\tau = 4.8$ and $\gamma\varepsilon_{ye} \approx 0.02$ μm for an initial emittance of $\gamma\varepsilon_{y0} \approx 150$ μm. This argument is not valid in the PDR where the extracted emittance is much larger and thus the alignment tolerances are looser. Even for $\varepsilon_{ye}/\varepsilon_y \approx 0.1$, the equilibrium emittance is $\gamma\varepsilon_{ye} \approx 15$ μm and alignment tolerances are $(15/0.02)^{1/2} \approx 30$ times looser (i.e., of order 1 mm rather than 30 μm [3]). Because alignment is not an issue in the PDR and the extracted beam stability can be attained in the MDR, a smaller value of N_τ (≈ 3.1), and therefore a simpler ring, can be accepted by choosing $\varepsilon_{ye}/\varepsilon_y \approx 0.1$ in the PDR.

IV. DAMPING TIME

The required store time Δt ($= N_\tau \tau_y$) should be shorter than the time between machine pulses (i.e., trains) $1/f$ increased by the number of stored bunch trains N_{train},

$$\tau_y = \frac{3C}{r_e c \gamma^3 I_2} \le \frac{N_{\mathrm{train}}}{f N_\tau}. \qquad (5)$$

Here, r_e is the classical electron radius, c is the speed of light, γ is the beam energy in units of mc^2, and I_2 ($= \sum_i \ell_i/\rho_i^2$) is the second synchrotron integral over the length ℓ_i and the radius ρ_i of each bend [8]. In an isomagnetic ring without wigglers, the damping time can be expressed as

$$\tau_y \approx \frac{(2.89 \times 10^{12}\ \mathrm{kG})C}{|B_a|\gamma^2 c} \frac{|\Theta_r|}{2\pi} \le \frac{N_{\mathrm{train}}}{f N_\tau}, \qquad (6)$$

where C is the ring circumference, c is the speed of light, B_a is the bend field of the arc dipole magnets in kG, and Θ_r is the total bending angle in the ring. For a racetrack ring with two 180° arcs, $\Theta_r = 2\pi$; however, in a “dog-bone” ring design, such as that considered for TESLA [9], Θ_r can be significantly larger.

At this point, we should note that the damping time *per se* is not the relevant parameter. Instead, we are concerned with the damping time scaled by the number of bunches in the ring which is roughly proportional to the ring circumference; two rings, one with twice the damping time but storing twice as many trains, will have the same damping performance. The damping requirement, Eq. (6), can be rewritten in terms of an “effective” damping time, which is independent of the ring circumference and depends only on the bunch train length and the separation between the trains,

$$\frac{\tau_y}{N_{\mathrm{train}}} \equiv \tau_{\mathrm{eff}} \approx \frac{(2.89 \times 10^{12}\ \mathrm{kG}) T_{\mathrm{train}}}{|B_a| \gamma^2} \frac{|\Theta_r|}{2\pi} \leq \frac{1}{f N_\tau} . \tag{7}$$

Here, T_{train} is the length of a bunch train plus the gap between trains,

$$T_{\mathrm{train}} = (N_b - 1)\tau_b + \tau_k , \tag{8}$$

where the bunch train has N_b bunches with a bunch spacing of τ_b and τ_k is a gap between the bunch trains to allow a kicker to rise or fall for injection and extraction. According to Eq. (7), to achieve $N_\tau > 4.8$ at 120 Hz with dipoles that are normal conducting iron magnets and $|B_a| \approx 18$ kG, the MDR energy must be $\gamma mc^2 \geq 2.83$ GeV. For reasons to be discussed in Sec. VIII, the energy of the NLC rings is chosen to be 1.98 GeV and the damping time is achieved by adding wiggler magnets to the straight sections.

V. RING CIRCUMFERENCE

At this point, we can specify the ring circumference. The ring's circumference C is set by the harmonic number h and the rf frequency f_{rf} and must be large enough to accommodate the N_{train} bunch trains,

$$C = hc/f_{\mathrm{rf}} \geq c N_{\mathrm{train}} T_{\mathrm{train}} . \tag{9}$$

As discussed in the previous section, the number of bunch trains stored simultaneously does not impact the damping requirements. Instead, the circumference is chosen large enough to allow for reasonable magnets in the arc cells and small enough not to unnecessarily increase the cost of the ring.

For the NLC main damping ring, $N_{\mathrm{train}} < 3$ sets the circumference too small for reasonable magnet strengths and $N_{\mathrm{train}} > 3$ generates a larger circumference than necessary. At $N_{\mathrm{train}} = 3$, and with the parameters of Table I, the MDR circumference must satisfy $C \geq 295.27$ m. Assuming an rf frequency of $f_{\mathrm{rf}} = 714$ MHz and $h = 708$ (evenly divisible by 2, 3, or 4 bunch trains for future flexibility), the circumference of the MDR is $C = 297.273$ m.

VI. WIGGLER DAMPING

Introducing a wiggler magnet into the ring generates more damping (i.e., an additive component to the I_2 synchrotron integral). With the definition

$$F_w \equiv I_{2w}/I_{2a} \geq 0 , \tag{10}$$

where I_{2w} is the sum $\Sigma_i \ell_i/\rho_i^2$ over the wiggler bends and I_{2a} is this sum over the arc bends, the effective damping time can be rewritten as

$$\tau_{\mathrm{eff}} \approx \frac{(2.89 \times 10^{12}\ \mathrm{kG}) T_{\mathrm{train}}}{|B_a| \gamma^2 (1 + F_w)} \frac{|\Theta_r|}{2\pi} . \tag{11}$$

The factor F_w represents the relative damping in the wiggler compared to that of the arcs. A ring without a wiggler has $F_w = 0$ while, for $F_w = 1$, the damping (or energy loss per turn) is equally shared between the arcs and the wiggler, and, for $F_w > 1$, the damping is dominantly achieved in the wiggler. A damping time of $\tau_y < 5.2$ msec ($\tau_{\mathrm{eff}} < 1.7$ msec) is achieved in the MDR at 1.98 GeV with $|B_a| < 18$ kG if $F_w > 1$. The second synchrotron integral in the arcs, I_{2a}, can be derived from the definition of I_2 and assuming a ring with a total of $|\Theta_r/\theta|$ identical bends, each bending by an angle θ,

$$I_{2a} = \left| \frac{\Theta_r}{2\pi} \frac{2\pi B_a}{(B\rho)} \right| . \tag{12}$$

Here, $(B\rho)$ is the standard energy dependent magnetic rigidity, $(B\rho) \approx 0.017\gamma$ (kG m). The second synchrotron integral in the wiggler, I_{2w}, can be written assuming a hard-edged wiggler field of B_w with dipoles occupying half the wiggler length, i.e., a filling factor of 50%,

$$I_{2w} \approx \frac{L_w B_w^2}{2(B\rho)^2} . \tag{13}$$

Note that Eq. (13) is actually valid for either a hard-edge model with a 50% filling factor or a sinusoidal model where B_w is the peak wiggler field. In practice, the filling factor depends on the wiggler period and gap and, for damping wigglers with a large ratio of period to gap, the filling factor can be significantly greater than 50%.

The active length of wiggler required for an isomagnetic arc is then taken from Eq. (5) with $I_2 = I_{2a} + I_{2w}$ and Eqs. (10), (12), and (13),

$$L_w \approx \frac{6C(B\rho)^2}{r_e c \tau_y \gamma^3 B_w^2} \frac{F_w}{1 + F_w} , \tag{14}$$

where $(B\rho)$ is proportional to γ. Equation (14) shows that the wiggler length reaches an asymptotic value for $F_w \gg 1$, in which case the wiggler does all the damping and the arcs do none. For the MDR parameters listed above at 1.98 GeV and $B_w = 21.5$ kG, a maximum wiggler length (i.e., $F_w \to \infty$) of $L_w \approx 66$ m is required. Conversely, the length is 33 m at $F_w = 1$. Before choosing a value for F_w, the effect of the wiggler on other parameters, including emittance and momentum compaction, must be considered.

VII. HORIZONTAL EMITTANCE

For a flat extracted beam, $\varepsilon_y \ll \varepsilon_x$, and several damping times, $N_\tau > 0.5 \ln(\varepsilon_{x0}/\varepsilon_x)$, the injected contribution to the horizontal emittance is typically damped to an insignificant level with respect to the equilibrium horizontal emittance. In this case, the equilibrium emittance is effectively the same as the extracted emittance and we can therefore ignore the injected horizontal emittance in what follows.

The horizontal equilibrium emittance generated in a ring can be written as [8]

$$\gamma \varepsilon_x = \frac{C_q \gamma^3 I_5}{J_x I_2} , \tag{15}$$

where $C_q \approx 3.84 \times 10^{-13}$ m, J_x $(= 1 - I_4/I_2)$ is the horizontal partition, and I_4 and I_5 are the fourth and fifth synchrotron integrals, respectively [8].

This can be written in a form that more explicitly illustrates the constraints using the effective damping time and assuming that there is no emittance contribution from the wiggler,

$$\gamma\varepsilon_x \approx \frac{3C_q}{2\pi r_e}\frac{T_{\text{train}}}{\tau_{\text{eff}}}\frac{\langle H\rangle_B}{J_x(1 + F_w)^2}, \tag{16}$$

where $\langle H\rangle_B$ is the average of the Courant-Snyder dispersion invariant over the arc bending magnets. This expression will be rederived in Sec. XII for the specific case of a TME lattice including the emittance contribution from the wiggler. However, at this point, it is worth noting that the emittance is determined by relatively few free parameters. The beam energy does not enter the expression, and the train length and effective damping time are specified by the performance requirements of the ring. Only J_x, F_w, and $\langle H\rangle_B$ depend on details of the specific lattice design. The damping partition J_x is normally very close to unity, but it can be changed using combined function bending magnets in the arcs. However, when $F_w \gg 0$, this method of changing J_x is not very effective. The damping partition can be expressed as

$$J_x = \frac{J_{x0} + F_w}{1 + F_w}, \tag{17}$$

where J_{x0} is the contribution from the arc cells alone. Clearly, as F_w increases, the fractional change in J_x becomes smaller.

VIII. RING ENERGY

There are a number of considerations when determining the ring energy. First, the desire to maintain high-spin polarization while damping the beams suggests that the nominal ring energy should be chosen so that the spin tune is a half integer. This limits the energy to

$$a\gamma = n + \tfrac{1}{2}. \tag{18}$$

Here, $a \equiv (g - 2)/2 \approx 1.16 \times 10^{-3}$ is the anomalous magnetic moment of the electron. At an energy $\gamma mc^2 \approx$ 1.98 GeV, the condition is met with $n = 4$. Second, we would prefer to keep the ring energy low in order to reduce ring costs as well as keep the normalized longitudinal emittance small, which makes bunch compression easier.

The problem with a low-energy ring is that it is harder to attain the required damping using reasonable magnet designs. We can understand the choices using the previous formulas. First, using Eqs. (11) and (14), and assuming that the fraction of damping due to the wigglers F_w and the wiggler peak field B_w are fixed, we find that, to meet the damping time requirements, the main bending field and the required length of wiggler scale as

$$B_a \propto \frac{1}{\gamma^2} \quad \text{and} \quad L_w \propto \frac{1}{\gamma}. \tag{19}$$

Thus, as the ring energy is increased, the bending magnets and wigglers become easier to design and construct.

Next, using Eq. (15), and noting that the I_5 integral scales as $I_5 \propto \theta^3/\rho$, we find that, to maintain the equilibrium emittance, the number of cells N_c and the bend magnet length L scale as

$$N_c \propto \gamma \quad \text{and} \quad L \propto \gamma^2. \tag{20}$$

Finally, given these relations, the circumference of the ring, the momentum compaction, and the synchrotron radiation power must scale as

$$C \propto \gamma^3, \quad a_p \propto \frac{1}{\gamma^2}, \quad \text{and} \quad P_{\text{rf}} \propto U_0 \propto \gamma, \tag{21}$$

where we assume that the cell length scales in the same manner as the length of the bends. The cost of the rings will tend to increase with the length and the number of cells, while the cost of the rf systems will increase with the power required; both of these costs will increase with higher energy. In addition, the momentum compaction decreases with the square of the ring energy while rough scaling for the longitudinal microwave threshold scales as $\gamma\alpha_p$. This suggests that longitudinal stability may be more difficult at higher energy.

Thus, the determination of the nominal ring energy becomes an optimization between the difficulty of the magnets and the packing of the cells versus the increase in size and cost of the ring. We have chosen an energy of 1.98 GeV and a spin tune of 4.5. This is the lowest energy that appears to yield reasonable designs for the bending and quadrupole magnets and the wigglers. Of course, during operation, we may want to vary the ring energy to optimize for a lower repetition rate or a larger injected emittance. For this reason, we are designing the rings to operate over the range of 1.9–2.1 GeV.

Finally, it is worth noting that intrabeam scattering does *not* present justification for increasing the ring energy. *When the effective damping times are held constant,* the emittance growth due to intrabeam scattering does not decrease with the ring energy [7]. Using a very simple scaling formula, the emittance growth depends upon the intrabeam scattering growth rate compared to the synchrotron radiation damping. The intrabeam scattering growth rate scales roughly as

$$\tau_{\text{IBS}}^{-1} \propto \frac{N\langle H\rangle}{\gamma\varepsilon_x\gamma\varepsilon_y\gamma\varepsilon_z}, \tag{22}$$

where N is the number of particles per bunch and $\langle H\rangle$ is the average of the dispersion invariant around the ring. The dispersion invariant scales as $\langle H\rangle \propto \theta^3\rho$ which, because the bending magnet field scales inversely with γ^2 while the number of cells increases with γ, as discussed in Eqs. (19) and (20), will be independent of energy. Thus, for given normalized emittances, the intrabeam scattering rate is independent of energy. In contrast, the damping rates are inversely proportional to the effective damping times multiplied by the number of bunch trains [Eq. (7)]. Since the ring circumference, and thus the number of bunch trains, increases as γ^3 [Eq. (21)], the damping rates scale inversely with γ^3. Finally, because the emittance growth due to intrabeam scattering depends on the scattering growth rate compared to the damping rate, the intrabeam scattering actually becomes worse as the design energy is increased.

IX. LATTICE CHOICES

At this point we should discuss the various lattice options. To attain the very low emittances needed in a future collider, the lattice should be efficient and have a small I_5 integral for a given bending magnet strength. Many possible lattice choices have been developed for the low emittance synchrotron radiation sources including the triple bend achromat (TBA) and the Chasman-Green lattice.

However, the needs of the damping rings are slightly different from that of the synchrotron radiation sources. In particular, one does not need many dispersion-free straight sections for insertion devices. In the damping rings, we need one dispersion-free region for injection and extraction and possibly another for a damping wiggler. The Chasman-Green and the TBA lattices were originally designed to have dispersion-free straight sections after every pair or every triplet of bending magnets, respectively. Although recently the lattices are sometimes reoptimized to attain better emittance performance by allowing dispersion between achromat cells, the lattices are not really optimized to create compact and efficient 180° arcs consisting of many cells. For this reason, we will consider only the TME [5] lattice for the damping rings. Actually, the TBA lattice essentially consists of a single TME cell with dispersion matching cells on either side. The TME lattice simply adds additional central cells before matching into the dispersion-free straight sections.

Another consideration is the choice of the horizontal damping partition number J_x. By using a combined function bend with a defocusing gradient, it is possible to increase J_x reducing the equilibrium horizontal emittance and increasing the horizontal damping rate. However, combined function magnets can be more difficult to align and have tighter field tolerances. Furthermore, as can be seen by examining Eq. (17), if the wiggler damping parameter F_w is significantly greater than zero, the relative gain from changing J_x is small. For this reason, we would only choose to use a combined function magnet if it simplifies the matching of the cell or has a better dynamic aperture. The design presented in this note is based on separated function magnets, although the previous NLC damping ring design, documented in Ref. [3], was based on combined function bending magnets.

X. TME LATTICE

A TME cell is composed of one bend of length L and angle θ and several (typically 3–4) quadrupole magnets. The horizontal beta β and dispersion η functions are a minimum in the center of the bend. For a TME cell with small angle bends ($\theta \ll 1$) and optical symmetry with respect to the middle of the bend magnet (i.e., $d\eta/ds = d\beta/ds = 0$ at bend center), the equilibrium emittance is, from Eq. (15),

$$\gamma\varepsilon_x \approx \frac{C_q\gamma^3}{J_x}\left[\frac{\eta^{*2}}{\beta^* L}\theta - \frac{\eta^*}{12\beta^*}\theta^2 + \left(\frac{\beta^*}{12L} + \frac{L}{320\beta^*}\right)\theta^3 + O(\theta^4)\right], \quad (23)$$

where β^* and η^* are the horizontal beta and dispersion functions at the center of the bend of length L. The emittance is minimum, $\gamma\varepsilon_{x_m}$, for an optimal set of functions, β_m^* and η_m^* [5] given by

$$\beta_m^* \approx \frac{L}{2\sqrt{15}}, \qquad \eta_m^* \approx \frac{L\theta}{24}, \qquad (24)$$
$$\gamma\varepsilon_{xm} \approx \frac{C_q\gamma^3\theta^3}{J_x 12\sqrt{15}}\left\{1 - \frac{(k\theta)^2}{23.33} + O[(k\theta)^4]\right\},$$

where $k^2 \equiv (1 + K_1\rho^2)$, K_1 is the normalized gradient in the bending magnet, and the damping partition is given by Eq. (17) where the arc contribution J_{x0} is

$$J_{x0} \approx 1 - \frac{(k\theta)^2}{6} + O[(k\theta)^4]. \qquad (25)$$

Notice that, although J_{x0} can be changed from unity with a combined function bending magnet, the change in J_x is reduced by the factor $(1 + F_w)$ as shown in Eq. (17). Although the emittance can be decreased with a defocusing gradient in the bending magnet (provided $F_w < 3$), the decrease is quite small unless the gradients are very large and F_w is small. In the previous NLC damping ring design [3] with $F_w \approx 1$, a defocusing gradient of 126 kG/m decreased the emittance by roughly 10%. *Thus, a combined function bending magnet makes sense only to the extent that it helps the matching in the TME cells.*

The cell can be "detuned" with respect to the optimum of Eq. (24) to increase the dispersion function; this will reduce the strengths of the quadrupoles and the chromatic correction sextupoles and potentially increase the ring's dynamic aperture. The unitless detuning factor, $\varepsilon_r \equiv \varepsilon_x/\varepsilon_{x_m} \geq 1$, is expressed as a function of the relative optical functions, $\beta_r \equiv \beta^*/\beta_m^*$ and $\eta_r \equiv \eta^*/\eta_m^*$ [4],

$$\varepsilon_r = \frac{5}{8}\frac{\eta_r}{\beta_r}[\eta_r - 2] + \frac{9}{2}\left[\frac{1}{4\beta_r} + \frac{\beta_r}{9}\right]. \qquad (26)$$

Equation (26) is plotted on a log-log scale in Fig. 2 (as in Ref. [4]) as η_r versus β_r for five different values of the relative emittance, ε_r (= 2, 4, 8, 16, and 32). From Fig. 2, a maximum in η_r can be found at a unique value of β_r

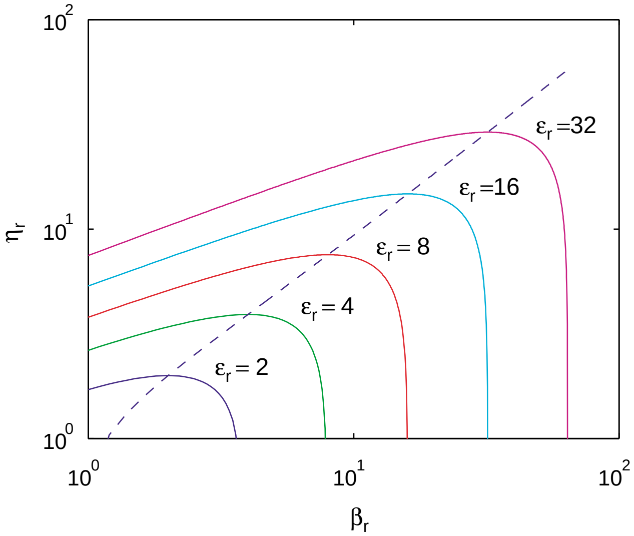

FIG. 2. (Color) Relative dispersion η_r versus relative beta function β_r at the center of bend in TME cell for five different values of the emittance detuning factor ε_r (= 2, 4, 8, 16, and 32). The dashed curve follows the maximum values of η_r and relates to Eq. (27).

for a given value of ε_r. With η_r maximized (i.e., $d\eta_r/d\beta_r = 0$), the optimal relative functions and detuned emittance scale with ε_r as

$$\beta_r = \varepsilon_r, \qquad \eta_r = 1 + \frac{2}{\sqrt{5}}\sqrt{\varepsilon_r^2 - 1}, \qquad \gamma\varepsilon_x \approx \varepsilon_r \frac{C_q\gamma^3}{J_x}\frac{\theta^3}{12\sqrt{15}}, \tag{27}$$

and

$$J_{x0} \approx 1 - \frac{(k\theta)^2}{12}(1 + \varepsilon_r) + O[(k\theta)^4], \tag{28}$$

where we have ignored the effect of a gradient in the dipole on the emittance since it has little effect. The maximum value of η_r moves along the dashed line of Fig. 2 for different values of ε_r. The functions required in the bend center are then given by Eqs. (24) and (27) as

$$\beta^* = \varepsilon_r \frac{L}{2\sqrt{15}}, \qquad \eta^* = \frac{L\theta}{24}\left[1 + \frac{2}{\sqrt{5}}\sqrt{\varepsilon_r^2 - 1}\right]. \tag{29}$$

The detuning factor is chosen only after consideration of its impact on other ring parameters, such as momentum compaction, which will be described. Finally, the required emittance is attained by choosing the appropriate bend angle θ in Eq. (27) and, for a simple racetrack ring, the number of TME cells required is set by $N_c = |2\pi/\theta|$ or, in general, as $N_c = |\Theta_r/\theta|$.

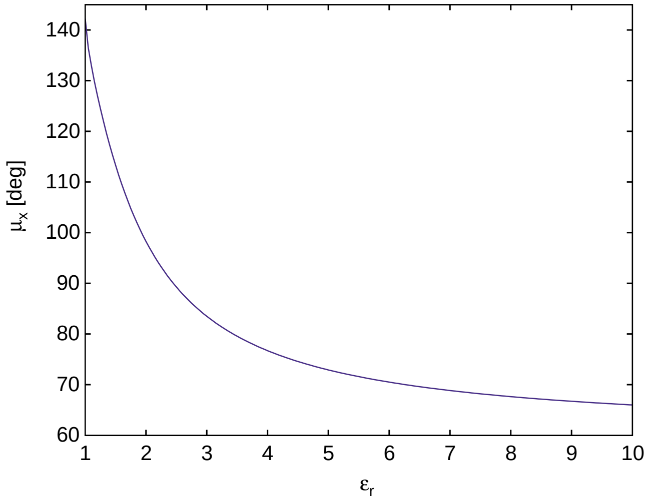

FIG. 3. (Color) Horizontal phase advance per $\frac{1}{2}$ TME cell as a function of the emittance detuning factor ε_r.

XI. EMITTANCE DETUNING FACTOR AND PHASE ADVANCE

By calculating the propagation of the periodic dispersion and its angle from the cell border to bend center, and including the conditions $\eta' = 0$ at both boundaries and $\eta = \eta^*$ at the bend center, the detuning factor ε_r can be shown [10] to be uniquely given by the horizontal phase advance per $\frac{1}{2}$ TME cell, μ_x,

$$\tan\mu_x = \frac{\sqrt{3}\,\varepsilon_r}{\sqrt{\varepsilon_r^2 - 1} - \sqrt{5}}. \tag{30}$$

Thus, a phase advance per $\frac{1}{2}$ TME cell of $\mu_x \approx 142°$ produces the smallest emittance of $\varepsilon_r = 1$. A value of $\varepsilon_r = \sqrt{6}$ is produced with a 90° per $\frac{1}{2}$ cell phase advance. Similarly, as $\varepsilon_r \longrightarrow \infty$, the phase advance per $\frac{1}{2}$ cell approaches 60°. We summarize this relationship in Fig. 3. Therefore, in choosing the emittance detuning factor we are simply choosing the horizontal phase advance per $\frac{1}{2}$ cell. The specific choice of values for ε_r is reserved for the next sections, where its impact on other ring characteristics is studied.

XII. HORIZONTAL EMITTANCE WITH A WIGGLER

The addition of a wiggler increases the damping rate and adds a component to the equilibrium emittance. By expanding the I_2 and I_5 synchrotron integrals in Eq. (15), the net equilibrium emittance of the ring is written as

$$\gamma\varepsilon_x \approx \gamma\varepsilon_a \frac{J_{x0}}{J_{x0} + F_w} + \gamma\varepsilon_w \frac{F_w}{J_{x0} + F_w}, \tag{31}$$

for a typical wiggler with small bend angle per half-period ($\theta_w \ll 1$). Here, $\gamma\varepsilon_a$ is the equilibrium emittance produced by the arcs in the absence of a wiggler, given by

Eq. (27) for TME cells, $\gamma\varepsilon_w$ is the emittance produced by the wiggler for $F_w \to \infty$, and J_{x0} is the horizontal damping partition number of the arcs (without a wiggler) and is given by Eq. (28) for TME cells; with no field gradient in the arc dipoles $J_{x0} \approx 1$.

The emittance produced by the wiggler can be approximately calculated using Eq. (15) and a hard-edged wiggler field model with period λ_w and peak field B_w,

$$\gamma\varepsilon_w \approx C_q\gamma^3 \frac{|B_w^3|\lambda_w^2\langle\beta_x\rangle}{192(B\rho)^3}. \tag{32}$$

The average horizontal beta function $\langle\beta_x\rangle$ through the wiggler is used here and assumed to fit the trivial condition $\langle\beta_x\rangle \gg \lambda_w/2\pi$. Substituting into Eq. (31) for $\gamma\varepsilon_a$ and $\gamma\varepsilon_w$ from Eqs. (27) and (32), respectively, gives the net horizontal equilibrium emittance of the ring, including wiggler,

$$\gamma\varepsilon_x \approx \frac{C_q\gamma^3}{12(J_{x0} + F_w)}\left[\frac{\varepsilon_r\theta^3}{\sqrt{15}} + \frac{F_w|B_w^3|\lambda_w^2\langle\beta_x\rangle}{16(B\rho)^3}\right]. \tag{33}$$

This approximation ignores the details of the dispersion suppressor optics at the start and end of the arcs, but is still a fairly accurate description, especially when the number of TME cells per arc is large (e.g., >10).

Note that the wiggler component of the emittance varies with the cube of its peak field and the square of its period. Since the length of the wiggler also varies inversely with the square of its peak field [see Eq. (14)], a weak field is not an advantage. However, reducing the wiggler period, within reasonable field limits, is useful. The Halbach scaling for hybrid wigglers [11] provides a useful starting point. It describes a limit on the peak field B_w in terms of the wiggler full gap g and the wiggler period λ_w,

$$B_w\ [\mathrm{kG}] \le 34.4\exp\left[-\frac{g}{\lambda_w}\left(5.08 - 1.54\frac{g}{\lambda_w}\right)\right], \tag{34}$$

which is roughly valid over the interval $0.08 < g/\lambda_w < 0.7$. At a value of $g/\lambda_w \approx 0.08$ the peak field might achieve 21.5 kG. This means that a gap of $g \approx 2$ cm requires a period of $\lambda_w \approx 25$ cm. The details of a realistic wiggler design constitute a separate study; however, these parameters are very close to the BL-9 wiggler installed in the SPEAR storage ring at SLAC [12] which is a Nd-B-Fe hybrid wiggler. It has a peak field of roughly 20.5 kG and a filling factor >50% which gives it the damping properties of a sinusoidal wiggler with peak field of 21.5 kG.

The mean beta function $\langle\beta_x\rangle$ through the wiggler can be kept reasonably small by segmenting the wiggler and adding quadrupole magnets at the segment gaps. The mean beta function is then approximately twice the length of these modular wiggler segments (for a 90°/cell wiggler FODO lattice). It is therefore useful to keep the lengths of the wiggler segments relatively short (e.g., 2 m) and maintain a horizontal phase advance in the region of ~90°/cell through the wiggler using a FODO-cell lattice. With multiple FODO cells, the ring tunes are easily varied over a significant range by adjusting the phase advance per cell of the wiggler focusing lattice. Maintaining a range of approximately 90°–120°/cell in 10 cells then allows a horizontal tune adjustment range of ±0.4 without a significant variation in the horizontal emittance. The vertical tune adjustment can be even larger. Figure 4 shows the relative horizontal equilibrium emittance of the NLC MDR ring, as a function of horizontal phase advance per wiggler FODO cell calculated using MAD [13]. A phase advance per wiggler FODO cell of 108° is about the minimum emittance.

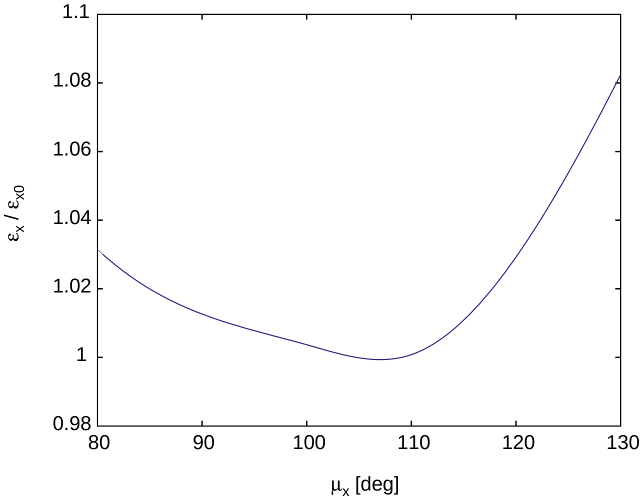

FIG. 4. (Color) Relative horizontal emittance as a function of horizontal phase advance per wiggler FODO cell calculated with MAD [13]. The vertical phase advance per FODO cell is held constant at $\mu_y = 72°$ and $\gamma\varepsilon_{x0} = 3\ \mu$m.

XIII. TME CELL DESIGN

The bend angle of a TME-cell dipole magnet is given by solving Eq. (33) for θ. The number of TME cells required, N_c, is then set as $N_c = |\Theta_r/\theta|$ where Θ_r is the total bending in the arc cells,

$$N_c \approx |\Theta_r|\gamma\left(\frac{\varepsilon_r}{\sqrt{15}}\right)^{1/3}\left[\frac{12\gamma\varepsilon_x}{C_q}(J_{x0} + F_w) - \frac{F_w|B_w^3|\lambda_w^2\langle\beta_x\rangle}{16}\left(\frac{\gamma}{(B\rho)}\right)^3\right]^{-1/3}. \tag{35}$$

The number of cells per ring is kept small by choosing small ε_r (shown in Fig. 8). The TME cell is composed of three or four quadrupoles and one dipole magnet. The dipole field B_a is given by Eq. (11) and its bend angle θ is based on the emittance in Eq. (33), so the length of the dipole magnet is uniquely defined by $L = |\theta(B\rho)/B_a|$. The values for β^* and η^* are given by Eq. (29), and the cell drift lengths and quadrupole strengths (one focusing and one defocusing family) are solved for in a nonlinear fit to produce the necessary values for β^* and η^* in the

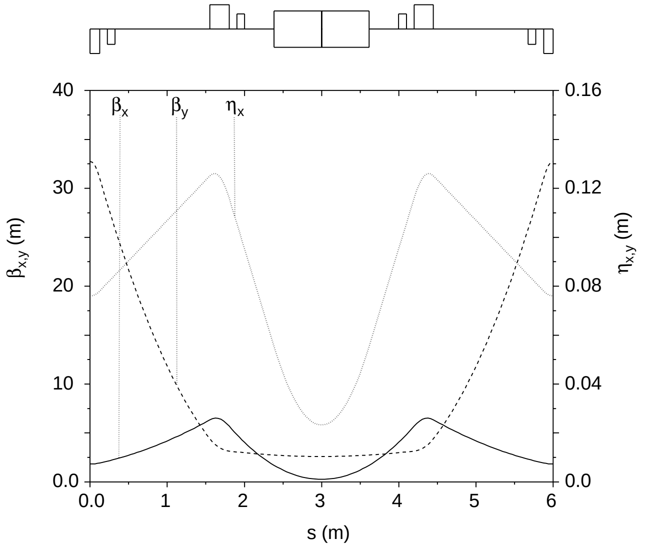

FIG. 5. Optical functions of a three-quad TME cell for the NLC MDR with separated function magnets. Magnet layout is indicated at the top with the bend in the center and quadrupoles shown larger than sextupoles.

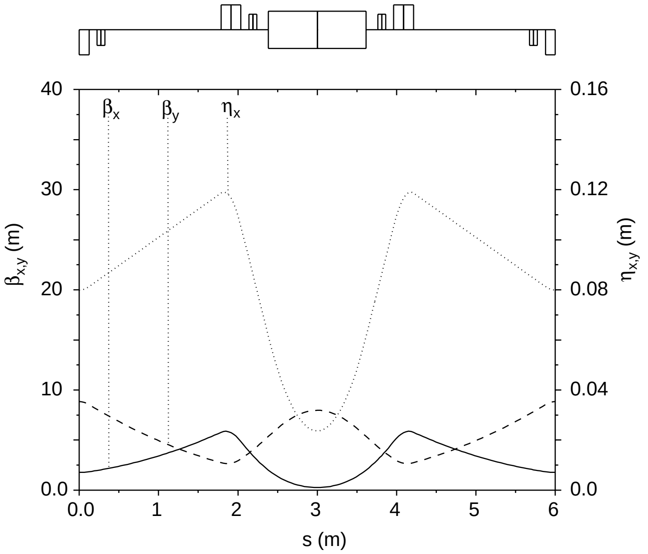

FIG. 6. Optical functions for the same three-quad TME cell as in Fig. 5 assuming a defocusing gradient of 66 kG/m in the bending magnet.

bend center. Figure 5 shows an example of a three-quad TME cell and its optical functions for the MDR assuming no gradient in the bending magnet while Fig. 6 shows the same cell but now assuming a defocusing gradient of 66 kG/m in the bending magnet. In both cases, the phase advances per $\frac{1}{2}$ cell are $\mu_x = 108°$ and $\mu_y = 36°$, and the magnet locations are depicted graphically at the top with the bend magnet in the center.

The PDR, with its very large injection emittance, is better suited to a four-quad TME cell. The four-quad cell produces smaller beta function peaks and thus leads to a smaller peak beam size. Figure 7 shows a four-quad TME cell for the PDR where the vertical beta function peaks at $\sim$32 m rather than $>$60 m in a similar three-quad design.

It is also possible to generate a TME cell with quadrupole gradients reversed from those indicated in Figs. 5–7. The reversed polarity cell has horizontally defocusing magnets located near the bend. Such cells have been applied to the MDR and generally produce weaker quadrupoles and larger dispersion in the nearby sextupoles. This may be an advantage for increasing the dynamic aperture; however, this lattice is more similar to the FOBO lattice, which is similar to a FODO lattice except the defocusing quadrupole and the bending magnets on either side are replaced by a single combined function bending magnet. In this case, the cells are limited in achievable horizontal phase advance (or detuning factor). Since the horizontal beta functions in the reversed cell increase monotonically from bend center to cell boundary, as opposed to that of Fig. 5, the horizontal phase advance is limited to approximately 90° per $\frac{1}{2}$ cell [14]. This limits ε_r in the reversed cell to $\approx$2.5 which requires $\approx$35% more TME cells than for $\varepsilon_r = 1$ [see Eq. (35)]. The reversed polarity cell is therefore not considered further.

In the NLC racetrack design, each arc is composed of $N_c/2 - 1$ *full* length cells plus a half cell to start and another half cell to terminate the periodic dispersion function in the arc. The half cells are dispersion suppressors which include one half-length bend and are slightly modified from a perfect half cell in order to precisely match the periodic dispersion function of the arc. The length of a full cell is determined from the ring circumference, the number of cells per arc in Eq. (35), and the straight section length needed to comfortably fit the wiggler of Eq. (14). Short, adjustable beta-matching sections separate the straight sections from the dispersion suppressors. The final value for the phase advance per TME $\frac{1}{2}$ cell is determined by ε_r,

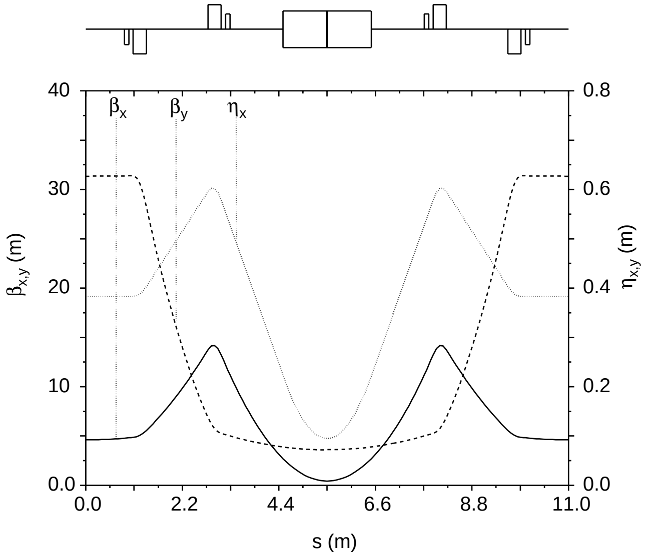

FIG. 7. Optical functions of a four-quad TME cell for the NLC PDR.

which is chosen based on arguments presented in the next sections.

XIV. MOMENTUM COMPACTION

Another goal of the design is to keep the momentum compaction α_p of the ring relatively large to avoid instability thresholds and the sensitivity to circumference changes. For the NLC MDR design, a somewhat arbitrary goal of $\alpha_p \geq 5 \times 10^{-4}$ has been set. The momentum compaction is given by [8]

$$\alpha_p = I_1/C\,, \tag{36}$$

where I_1 $(= \Sigma_i \ell_i \langle\eta\rangle_i/\rho_i)$ is the first synchrotron integral, C is the nominal ring circumference, and $\langle\eta\rangle_i$ is the mean dispersion function averaged over the length of the bend magnet. Using the midpoint dispersion η^* from Eq. (29) and the bend angle solved with Eq. (33) gives

$$\begin{aligned}\alpha_p \approx |\Theta_r|\,\frac{\pi}{2}\left(\frac{4\sqrt{15}}{9}\right)^{2/3}\frac{r_e\tau_{\rm eff}\gamma(1+F_w)^{5/3}}{CT_{\rm train}}\\ \times\left(\frac{\gamma\varepsilon_x}{C_q}-\frac{|B_w^3|\lambda_w^2\langle\beta_x\rangle\gamma^3}{192(B\rho)^3}\,\frac{F_w}{J_{x0}+F_w}\right)^{2/3}\\ \times\frac{\sqrt{5}+\sqrt{\varepsilon_r^2-1}}{\varepsilon_r^{2/3}}\,.\end{aligned} \tag{37}$$

The momentum compaction and the number of cells are plotted as functions of ε_r in Fig. 8, where it is also clear that $\varepsilon_r > 4$ amounts to $\approx$60% more TME cells than at $\varepsilon_r = 1$. The maximum momentum compaction, for a reasonable number of TME cells, is then located at $\varepsilon_r \approx 1.3$. To keep the momentum compaction large without adding a significant number of costly TME cells requires choosing ε_r near this peak. Equation (30) shows that $\varepsilon_r = 1.647$ is equivalent to a horizontal phase advance per $\frac{1}{2}$ cell of $\mu_x \approx 108°$. This judicious choice allows five TME cells to produce 6π of phase advance and, therefore, sextupole aberrations are more locally cancelled by optical symmetry. For these reasons, we choose $\varepsilon_r = 1.647$ which produces $\alpha_p/\alpha_{p0} \approx 1.14$ and $N_c/N_{c0} \approx 1.18$.

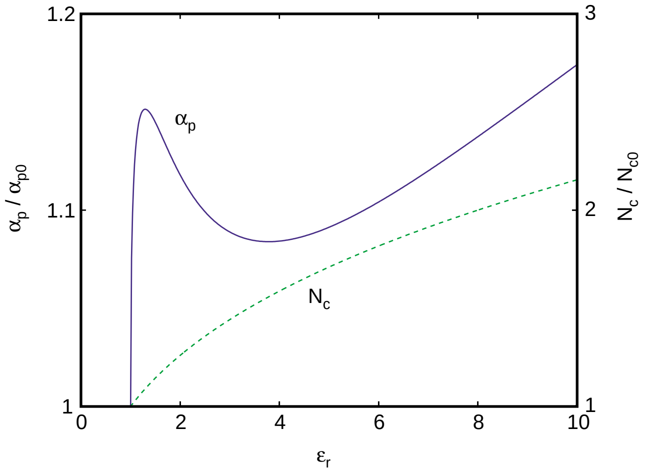

FIG. 8. (Color) Relative momentum compaction α_p/α_{p0} and relative number of TME cells N_c/N_{c0} plotted as a function of the "detuning" factor ε_r. The normalization of these relative curves is with respect to their values at $\varepsilon_r = 1$ [i.e., $\alpha_{p0} \equiv \alpha_p(\varepsilon_r = 1)$ and $N_{c0} \equiv N_c(\varepsilon_r = 1)$].

XV. DYNAMIC APERTURE AND TME CELL CHROMATICITY

While the dynamic aperture optimization is beyond the scope of this paper, we will discuss the approach that was used in optimizing the designs documented in Refs. [2,3] which is the same as that which we plan to follow for this design. First, the phase advance of the cells is chosen to minimize the first-order geometrics through the arcs. This fixes the tunes of the arcs, but the tunes of the ring can still be adjusted using the quadrupoles in the wiggler straight section. Second, we adjusted the position of the sextupoles to minimize the three second-order tune shifts with amplitude. Actually, in Ref. [3], this was done using three pairs of sextupoles in each cell; however, from the cost perspective, it would be desirable to simply use two pairs of sextupoles and optimize their locations.

The five first-order geometric aberrations from the sextupoles can be written as

$$\int_{\rm arc} ds\,\beta_x^{3/2}K_2e^{i(2\psi_x\pm\psi_x)}, \qquad \int_{\rm arc} ds\,\beta_x^{1/2}K_2e^{i(\psi_x\pm2\psi_y)}, \qquad \int_{\rm arc} ds\,\beta_x^{1/2}\beta_yK_2e^{i\psi}, \tag{38}$$

where K_2 is the normalized sextupole strength and the $\pm$ is used to denote two different phase advances; i.e., $(2\psi_x \pm \psi_x)$ denotes both $3\psi_x$ and ψ_x. Since the cells are periodic, these integrals can be minimized by making these phase advances through the arcs integral multiples of 2π. Assuming 15 arc cells plus the dispersion suppression cells, we have chosen a horizontal phase advance of 108° per half cell and a vertical phase advance of 36° per half cell. This choice cancels these first-order aberrations; however, it drives the octupole difference resonance, a second-order effect of the sextupoles. In practice, we found that this term can be minimized by choosing the location of the sextupoles and shifting the cell phase advances slightly from the optimal values described above.

Another issue is the effect of the wiggler magnets on the optics and the nonlinearities introduced by them. At lowest order, the wiggler field will perturb the linear optics, but this can be compensated using quadrupoles in and around the wiggler region. The next significant term is an octupolelike nonlinearity which scales as $L_w(B_w/\gamma\lambda_w)^2$ [15,16]; higher-order terms have additional factors of $1/\lambda_w$. These nonlinear terms can be important and must be considered in the design of the wiggler [17].

Another issue that was found to be very important when optimizing the dynamic aperture of the ring is to reduce the natural chromaticity of the cells. Unfortunately, there does not seem to be a simple analytic expression for the chromaticity in a TME cell. However, empirically, it was found that the chromaticity could be significantly reduced using a weak defocusing gradient in the bending magnets [18]. The horizontal and vertical chromaticities and the horizontal damping partition are plotted versus the gradient in the bending magnet for the 6 m TME cell for the NLC MDR in Fig. 9. Clearly, the vertical chromaticity decreases significantly as a defocusing gradient is added with an apparent minimum at roughly $K_1 \approx -1\ \mathrm{m}^{-2}$, which corresponds to a gradient of 66 kG/m. At the same time, the horizontal chromaticity is roughly constant and the horizontal damping partition J_{x0} increases from 1 to 1.5. The optics of the cell with a defocusing gradient of 66 kG/m in the bending magnet is shown in Fig. 6.

Next, the dependence of the chromaticities on the phase advance per cell is illustrated in Fig. 10. Here, we have plotted the TME cell detuning factor and the horizontal and vertical chromaticities per cell in the 6 m NLC MDR cell versus the horizontal phase advance where the vertical phase advance is matched to be $\frac{1}{3}$ of the horizontal. The two curves for the vertical chromaticity correspond to cells with and without a defocusing gradient of 66 kG/m—the horizontal values differ by only a few percent for the two cases and thus both are not plotted. Note that with a detuning factor of 1.64 and a cell tune of 0.6, the horizontal chromaticity is roughly 50% of the value when the detuning factor is 1.

Unfortunately, while both Figs. 9 and 10 are illustrative, they do not provide a direct connection to the dynamic aperture of the ring. For example, although the vertical chromaticity may be larger, cells with smaller defocusing gradients also have significantly weaker sextupoles to correct the chromaticity because of the larger beta functions at the sextupole locations. Thus, the results of Figs. 9 and 10 can provide some guidance, but, to the best of our knowledge, the final configuration to optimize the dynamic aperture must be chosen empirically. As previously mentioned, in the present design iteration, we have chosen to use a bending magnet without any gradient to compare with the performance of the previous design described in Ref. [3].

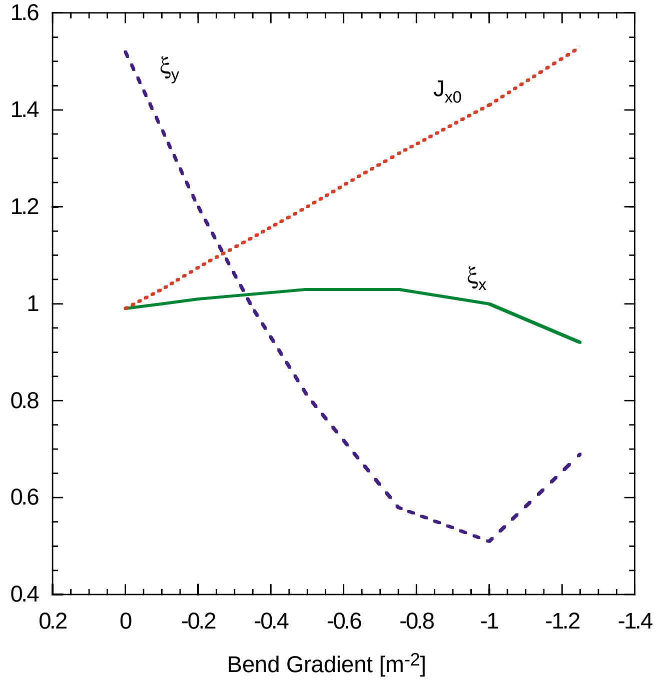

FIG. 9. (Color) Horizontal and vertical chromaticities and horizontal damping partition J_{x0} versus the gradient in the bending magnet of the 6 m NLC MDR cell.

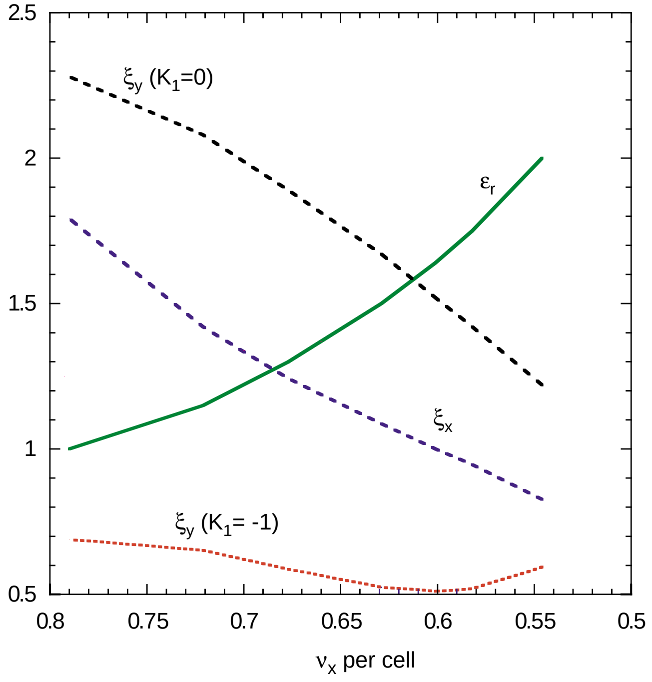

FIG. 10. (Color) TME cell detuning ε_r and the horizontal and vertical chromaticities versus the horizontal phase advance per cell in the 6 m NLC MDR cell; vertical phase advance is matched to be 1/3 of the horizontal. The vertical chromaticity is plotted for a cell with a defocusing gradient of 66 kG/m in the bending magnet and a cell without any gradient in the bending magnet.

XVI. LONGITUDINAL PHASE SPACE

Thus far, our discussion has concentrated on the transverse dynamics and requirements of the ring. In longitudinal phase space, the equilibrium rms relative energy spread σ_δ and rms bunch length σ_z (for zero current) are given by

$$\sigma_\delta = \sqrt{\frac{C_q I_3}{2I_2 + I_4}} \approx \gamma \left[\frac{C_q |B_a|}{(B\rho)} \frac{1 + F_w |\frac{B_w}{B_a}|}{3 - J_{x0} + 2F_w} \right]^{1/2}, \tag{39}$$

and

$$\sigma_z \approx C \sigma_\delta \sqrt{\frac{\alpha_p \gamma m c^2}{2\pi h e V_0 |\cos\varphi_0|}}, \tag{40}$$

where h $(= f_{\mathrm{rf}}C/c)$ is the ring's harmonic number, V_0 is the on-crest rf voltage in the ring, and φ_0 is the synchronous rf phase angle given by

$$\varphi_0 \approx \sin^{-1}\left(\frac{2\gamma mc^2 T_{\mathrm{train}}}{eV_0\tau_{\mathrm{eff}}}\right), \tag{41}$$

where we have expressed the energy loss per turn in terms of the beam energy, the effective damping time, and the length of the bunch train and kicker gap.

In general, the amount of damping required in the longitudinal plane is relatively small and thus the extracted longitudinal phase space is very close to the equilibrium value. The equilibrium rms energy spread depends only on the beam energy and the bending fields. A typical value is 0.1% which is a factor of 10 to 20 smaller than typical injected energy spreads. It is important to note that the equilibrium energy spread is insensitive to the value of F_w and depends only on the square root of the peak wiggler field and thus is not a significant factor when specifying the wiggler magnet; this will be illustrated more explicitly in Sec. XVII.

The equilibrium bunch length depends on the momentum compaction and the rf system. Usually, the equilibrium bunch length should be short to minimize the bunch compression after the damping ring. However, it is also desirable to keep the bunch length fairly long to reduce the peak current in the ring; this reduces the emittance growth due to intrabeam scattering and the Touschek scattering rate and increases the thresholds for the longitudinal single bunch instabilities. In the NLC damping rings, a bunch length of 4–5 mm should be sufficient for a peak bunch charge of 1.5×10^{10}.

The rf voltage should be chosen with a sufficient overvoltage to keep φ_0 relatively small. The rf frequency can be chosen to vary the bunch length for a given voltage and momentum compaction within the limit determined by the bunch spacing. In general, lower frequency rf systems will be more costly but will be more stable with smaller transverse and longitudinal impedances. In the NLC damping rings, we have chosen an rf frequency of 714 MHz, which is the lowest frequency consistent with a bunch spacing of 1.4 ns.

XVII. CHOICE OF WIGGLER LENGTH

The choice of relative wiggler strength F_w involves, in part, evaluating Eqs. (11), (14), (35), and (37) [i.e., damping time, wiggler length, number of cells, and momentum compaction]. If the arc bends are to have fields of $|B_a| < 18$ kG, then, for the MDR parameters of Table I at 2 GeV, the wiggler needs $F_w > 1$. The choice of F_w also impacts many other critical ring parameters, such as the momentum compaction and the beam energy spread, as described above.

Figures 11 and 12 show the momentum compaction α_p, active wiggler length L_w, arc dipole field B_a, and the wiggler's contribution to horizontal equilibrium emittance, $\Delta\gamma\varepsilon_w \equiv \gamma\varepsilon_w F_w/(J_{x0} + F_w)$, all plotted against the wiggler relative damping factor F_w. The parameters are those of the MDR at 1.98 GeV and with $C \approx 297$ m, $\tau_y \approx 5.2$ msec, $\lambda_w = 27$ cm, $\langle\beta_x\rangle \approx 4.5$ m, $B_w = 21.5$ kG, and $\varepsilon_r = 1.647$. The momentum compaction increases fairly rapidly with F_w while the wiggler length increases asymptotically (Fig. 11). The arc dipole fields B_a are reasonable, at 2 GeV, for $F_w > 1$, but the wiggler's contribution to the horizontal equilibrium emittance increases with increasing F_w (Fig. 12). An increase in emittance requires reducing the arc bend angles and adding TME cells.

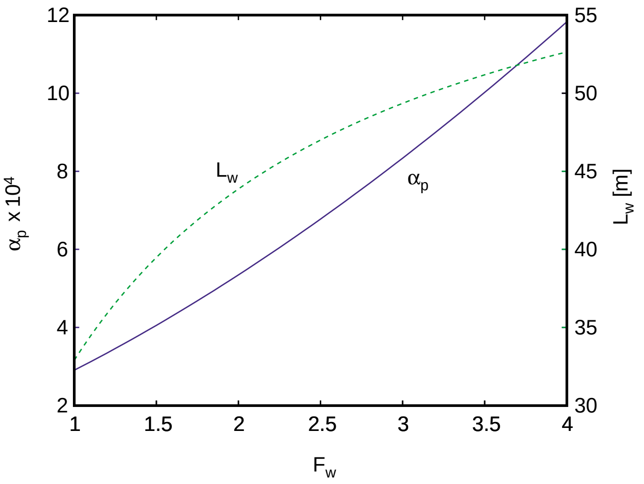

FIG. 11. (Color) Momentum compaction α_p and wiggler length L_w plotted versus wiggler damping F_w.

Finally, the extracted energy spread and bunch length are plotted in Fig. 13 as a function of F_w using the same MDR parameters as in Figs. 11 and 12 and an rf voltage of $V_0 = 1.5$ MV with a harmonic number of $h = 708$. For the MDR design, a value for $F_w = 2.3$ is chosen in order

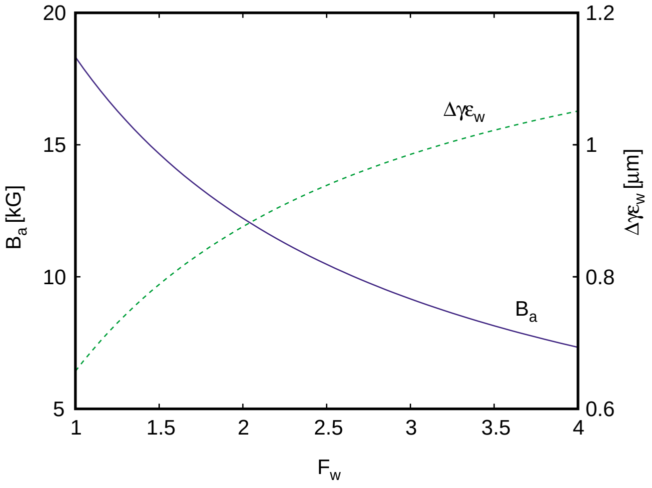

FIG. 12. (Color) Arc dipole field B_a and wiggler's emittance contribution $\Delta\gamma\varepsilon_w$ plotted against F_w.

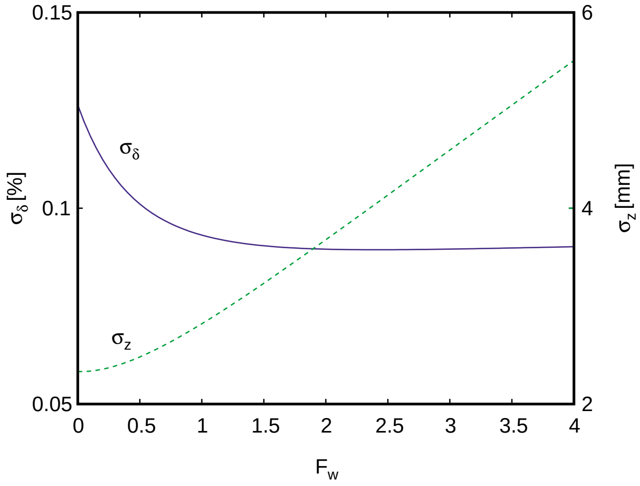

FIG. 13. (Color) MDR extracted energy spread σ_δ and bunch length σ_z plotted against F_w.

to keep $\alpha_p > 5 \times 10^{-4}$ and to produce a bunch length of 4 mm rms at $V_0 = 1.5$ MV. The active wiggler length at $F_w = 2.3$ is then $L_w \approx 46$ m and the arc bend fields are a modest 11 kG.

XVIII. TUNES

The choice of ring tunes depends on a number of factors including the dynamic aperture and the tolerance sensitivities. Since most linear collider designs specify "flat" beams with $\gamma\varepsilon_x \gg \gamma\varepsilon_y$, there are usually tight tolerances to limit the residual betatron coupling as well as the vertical dispersion. These tolerances are proportional to $|\sin\pi\nu_y|$ and $|\sin\pi\nu_\pm|$ where $\nu_\pm = \nu_x \pm \nu_y$ and, thus, to avoid unnecessarily tight tolerances, we need to restrict the operational tune space. Figure 14 is a plot, from Ref. [19], of the tune diagram where we have restricted $|\Delta\nu_y| > 0.17, |\Delta\nu_\pm| > 0.15$ and kept a reasonable distance from the horizontal integer and half-integer resonances; resonance lines up to order of the normal sextupole are included for reference, and the shaded regions are not desirable. Finally, we should note that the tune adjustment in the ring is most easily performed in the wiggler and injection/extraction straight sections where the tunes can be adjusted by more than an integer without impact to the emittance or the ring operation.

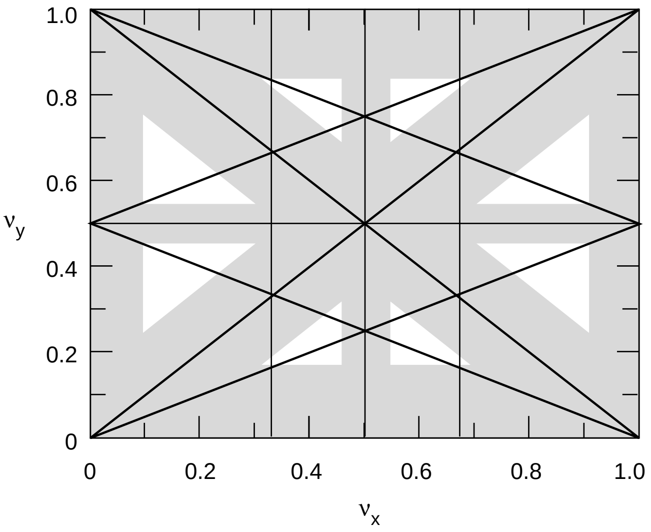

FIG. 14. Tune space with restrictions due to coupling and vertical dispersion.

XIX. DESIGN COMPLETION

With the choices made for F_w and ε_r, the remainder of the ring can be laid out. The length of a TME cell L_c is calculated (for the MDR) using

$$L_c = (C - L_w - L_{\mathrm{inj/ext}} - 2\Delta L)/N_c\,, \qquad (42)$$

where ΔL (> 0) is the additional straight section length which is included in order to provide space for the arc-to-straight matching sections and the rf systems and $L_{\mathrm{inj/ext}}$ is the length required for the injection and extraction regions. In the MDR the wiggler is situated on one side of the ring while the injection, extraction, and rf systems are on the opposite side. In contrast, the PDR includes a half-length wiggler on each side of the ring allowing more room for the optics surrounding the PDR injection kicker which is a difficult magnet due to the very large incoming e^+ beam size (see Figs. 15 and 16).

The length of the modular wiggler segments and the length of the drifts between segments must be determined with a detailed wiggler design. For this study, we assume a 2.3 m wiggler segment length and a 36 cm intersegment drift space which includes a 15 cm long quadrupole magnet. The wiggler then requires 20 segments. This sets a lower limit on ΔL of 20×0.36 m $= 7.2$ m. The final value of ΔL is set by considering the space required for the matching sections. This is arrived at by running the computer program MAD [13] which minimizes the quadrupole strengths and beta functions through the matching sections. For the NLC MDR, a value of $\Delta L \approx 12.2$ m is used. The TME cell length is then 6.0 m with 15 cells per arc. This generates an equilibrium horizontal emittance of $\gamma\varepsilon_x \approx 3.0$ μm [see Eq. (33)]. With the cell length known, the TME cell is fitted using a three-quadrupole cell (as in Fig. 5) with the cell phase advances, the dispersion, and the beta functions constrained at the bend center. For the MDR, the quadrupole pole-tip fields are very reasonable at 5.9 and -4.6 kG for 25 cm long magnets with 20 mm radii. In contrast, the PDR TME cells are formed using four quadrupole magnets as shown in Fig. 7. This reduces the peak value of the beta functions which, with the very large input emittance of the PDR, better controls the peak transverse beam size through the arcs.

This verifies the MDR selection of $N_{\mathrm{train}} = 3$ bunch trains. If the MDR is redesigned with $N_{\mathrm{train}} = 2$ trains,

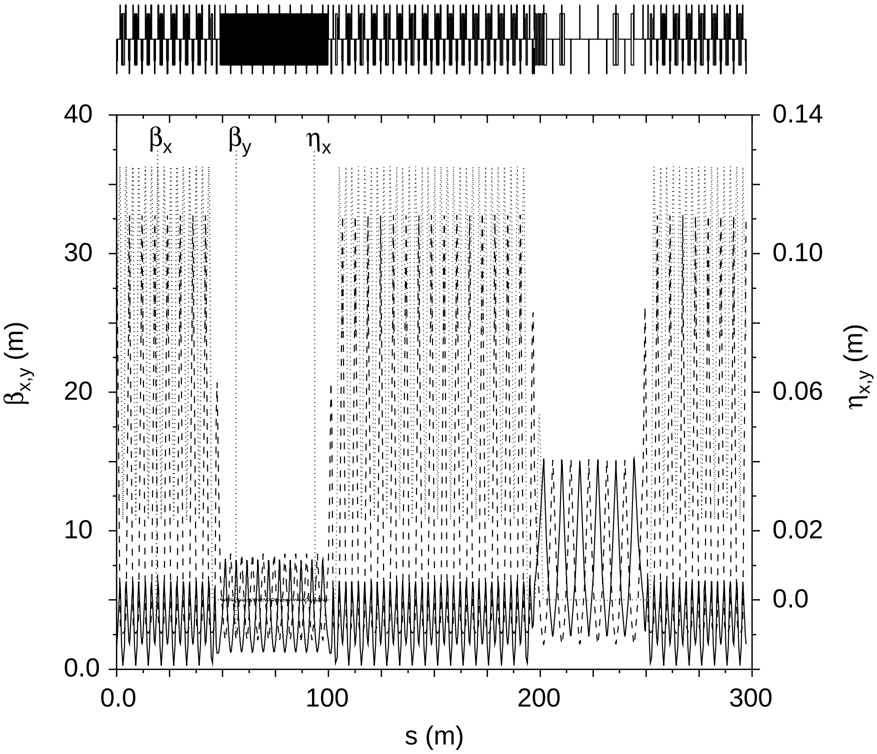

FIG. 15. Optical functions of the entire MDR. The wiggler is the darkened area at $s \approx 50-100$ m.

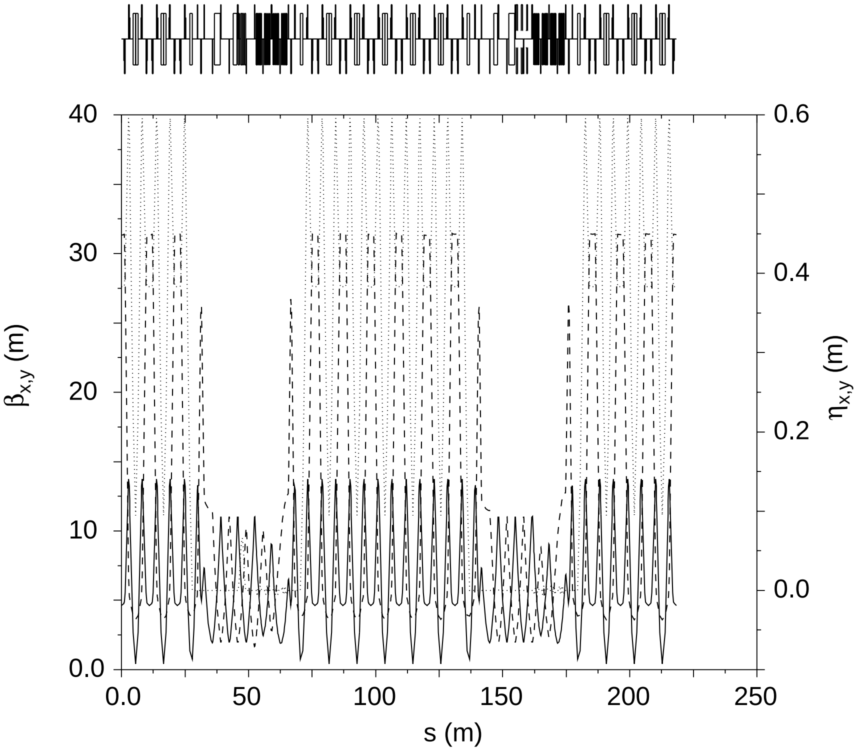

FIG. 16. Optical functions of the entire PDR. The wigglers are the two darkened areas.

TABLE II. List of NLC MDR and PDR parameters for the collider parameters of Table I.

Parameter	Symbol	PDR	MDR
Nominal electron/positron ring energy [GeV]	γmc^2	1.98	1.98
Number of bunch trains stored	N_{train}	2	3
Store time/train in units of damping time const.	N_τ	3.1	4.8
Ring circumference [m]	C	218	297
Ratio of y-equilibrium to y-extracted emittance	$\varepsilon_{ye}/\varepsilon_y$	0.1	0.67
Extracted horizontal emittance (norm., rms) [μm]	$\gamma\varepsilon_x$	150	3
Extracted vertical emittance (norm., rms) [μm]	$\gamma\varepsilon_y$	100	0.03
Vertical damping time ($\tau_y \approx \tau_x$) [ms]	τ_y	5.4	5.2
Ratio of energy loss in wiggler to that in arcs	F_w	0.5	2.3
Peak field of wiggler [kG]	B_w	21.0	21.5
Wiggler period [cm]	λ_w	100	27
Net active wiggler length (w/o segment gaps) [m]	L_w	16	46
Emittance detuning factor	ε_r	1.65	1.65
Momentum compaction [10^{-4}]	α_p	40	6.6
Harmonic number	h	520	708
Extracted energy spread (rms) [10^{-4}]	σ_δ	8.9	8.9
Energy loss per turn [MeV]	U_0	0.53	0.76
Extracted bunch length (rms at $V_0 = 1.5$ MV) [mm]	σ_z	8.1	4.0
Number of quadrupole magnets per TME cell		4	3
Number of TME cells/arc ($N_c - 1$ *full* cells/arc)	N_c	6	15
TME cell length [m]	L_c	11	6.0

the circumference is reduced to 198 m, but the cell length is reduced to 2.8 m. The two-train MDR is designed for the same momentum compaction as the three-train MDR (by reducing $F_w = 1.7$), which keeps the wiggler length nearly constant, but the same length and radii quadrupole magnets now require pole-tip fields > 12 kG. The dispersion in the sextupoles is also reduced and it is expected that the dynamic aperture will suffer. For these reasons we choose $N_{\text{train}} = 3$ bunch trains for the MDR and $N_{\text{train}} = 2$ bunch trains for the PDR. A list of MDR and PDR parameters is given in Table II. A list of various magnet parameters is also included in Table III and the entire MDR and PDR rings are shown in Figs. 15 and 16, respectively.

It should be noted that the MDR energy can be increased to 2.8 GeV and attain the necessary damping and emittance values while eliminating the need for a wiggler altogether. This is an interesting possibility, but in this case the momentum compaction for a three-train MDR ring is reduced to 1.6×10^{-4}, which is thought, at the present time, to be too small. The higher energy also forces the number of cells to be doubled (i.e., 30 per arc) and pushes the energy loss per turn above 1 MeV. The TME quadrupoles also require nearly twice the field strength, and the dispersion in the sextupoles is reduced due to the shorter cells. For these reasons, we choose an energy of 1.98 GeV for both rings, which requires a wiggler in each ring.

Alternate ring layouts can also be explored. One possibility is a dog-bone ring, similar to the DESY damping ring [9], where each arc includes 360° of bending rather than the racetrack with 180° per arc. The increased bending can be used to eliminate the wiggler, even at 2 GeV. Unfortunately, the number of TME cells more than doubles and the cell lengths are halved. In the MDR, this forces unrealistically strong quadrupole strengths, small dispersion in the sextupoles, and a momentum compaction value of $\sim 4 \times 10^{-4}$. This scheme has not been pursued further for the NLC designs.

Finally, tunable four-dipole chicanes have been added to the straight sections to allow empirical corrections of

TABLE III. List of various magnet parameters in the NLC MDR and PDR.

Parameter	Symbol	PDR	MDR
Length of arc dipole magnet (full length) [m]	L	2.01	1.23
Field of arc dipole magnets (full and half length) [kG]	B_a	17.2	11.25
Bend angle of full length dipole magnets [deg]	θ	30	12
Length of arc quadrupole magnets [m]	L_Q	0.30	0.25
Pole-tip radius of arc quadrupole magnets [mm]	r_Q	50	20
Field of focusing (inner) arc quadrupole magnets [kG]	B_{QF}	+7.2	+5.9
Field of defocusing (outer) arc quadrupole magnets [kG]	B_{QD}	−3.9	−4.6

the ring circumference (at $s \sim 200$ m in Fig. 15 and $s \sim 40$ m in Fig. 16) [6]. Since the ring rf frequency needs to be locked to the extraction linac, we employ a magnetic chicane to make small circumference corrections against possible ground motion or temperature induced variations. The critical ring parameters are not significantly affected by the chicanes.

XX. CONCLUSIONS

The design for a damping ring using TME cells can be fairly well determined by the emittance reduction requirements, the collider repetition rate, the number and spacing of the bunches in a train, and kicker bandwidth limitations. Other concerns such as momentum compaction, wiggler length, bunch length, and limiting the number of components can be included to produce a relatively unique design. A computer program has been written to quickly generate complete ring parameter sets for various collider and injector schemes. Although guides are provided based on previous experience, the final choice of tunes and type of sextupole compensation is best left to future dynamic aperture studies. Collective effects have not been considered here.

ACKNOWLEDGMENTS

We would like to thank R. Brinkmann, W. Decking, H. Nishimura, L. Rifkin, D. Robin, M. Ross, R. Ruth, and Y. Wu for many useful and entertaining conversations. This work was performed under U.S. Department of Energy Contract No. DE-AC03-76SF00515.

[1] SLAC Report No. SLAC-Report-95-471, 1995, edited by G. A. Loew.

[2] T. O. Raubenheimer, L. Z. Rivkin, and R. D. Ruth, in *Proceedings of Snowmass 1988, Snowmass, Colorado* (World Scientific, Singapore, 1988), p. 620.

[3] SLAC Report No. SLAC-Report-474, 1996, edited by T. O. Raubenheimer.

[4] J. P. Potier and L. Rivkin, CERN Report No. CERN-PS-97-020, 1997.

[5] L. C. Teng, Fermilab Report No. TM-1269, 1984.

[6] P. Emma and T. O. Raubenheimer, in *Proceedings of the 1999 IEEE Particle Accelerator Conference, New York* (IEEE, Piscataway, NJ, 1999), Vol. 5, pp. 3438–3440.

[7] T. O. Raubenheimer, SLAC Report No. SLAC-387, 1991.

[8] R. Helm *et al.*, in *Proceedings of the 1973 IEEE Particle Accelerator Conference, San Francisco* (IEEE, Piscataway, NJ, 1973), p. 900.

[9] K. Floettmann and J. Rossbach, in *Proceedings of the 1994 European Particle Accelerator Conference, London* (World Scientific, Singapore, 1994), p. 509.

[10] L. Rivkin, in *Proceedings of the 7th International Workshop on Linear Colliders (LC97), Zvenigorod, Russia, 1997* (INP, Provino, Russia, 1997), p. 644.

[11] G. Brown, K. Halbach, J. Harris, and H. Winick, Nucl. Instrum. Methods Phys. Res. **208A**, 65 (1983).

[12] Michael Baltay (private communication).

[13] H. Grote and F. C. Iselin, CERN Report No. CERN/SL/90-13 (AP) Rev. 3, 1993.

[14] This was studied numerically and an approximate analytical argument was provided by J. Murphy at BNL.

[15] Lloyd Smith, in *Proceedings of the 13th International Conference on High Energy Accelerators, Novosibirsk, USSR, 1986* (Nauka, Novosibirsk, 1987).

[16] W. Decking, Doctoral thesis, Hamburg University, Hamburg, Germany, 1995.

[17] J. Corlett *et al.*, SLAC technical note No. LCC-0031, 1999 (unpublished).

[18] H. Nishimura, D. Robin, and Y. Wu (private communication).

[19] T. O. Raubenhemier *et al.*, Nucl. Instrum. Methods Phys. Res., Sect. A **335**, 1 (1993).